



# Temperature dependent product distribution of electrochemical CO<sub>2</sub> reduction on CoTPP/MWCNT composite

M.N. Hossain<sup>a,1</sup>, P. Prslja<sup>b,1</sup>, C. Flox<sup>a</sup>, N. Muthuswamy<sup>a,c</sup>, J. Sainio<sup>d</sup>, A.M. Kannan<sup>e</sup>,  
M. Suominen<sup>a</sup>, N. Lopez<sup>b</sup>, T. Kallio<sup>a,\*</sup>

<sup>a</sup> Department of Chemistry and Materials Science, Aalto University School of Chemical Engineering, P.O. Box 16100, FI-00076 Aalto, Finland

<sup>b</sup> Institute of Chemical Research of Catalonia, ICIQ, The Barcelona Institute of Science and Technology, AV. Paisos, Catalans, 16, 43007 Tarragona, Spain

<sup>c</sup> Department of Chemical Engineering, Norwegian University of Science and Technology, Sem Sælands vei 4, N-7491 Trondheim, Norway

<sup>d</sup> Department of Applied Physics, Aalto University School of Science, P.O. Box 15100, FI-00076 Aalto, Finland

<sup>e</sup> Ira. Fulton School of Engineering, Arizona State University, P.O. Box 879309, Tempe, AZ 85287-9309, USA

## ARTICLE INFO

### Keywords:

Electrochemical CO<sub>2</sub> reduction  
Co-based molecular catalyst  
Multiwalled carbon nanotube  
Temperature selectivity dependence

## ABSTRACT

Electrochemical reduction of CO<sub>2</sub> to valuable products on molecular catalysts draws attention due to their versatile structures allowing tuning of activity and selectivity. Here, we investigate temperature influence on CO<sub>2</sub> conversion product selectivity over a Cobalt(II)-tetraphenyl porphyrin (CoTPP)/multiwalled carbon nanotube (MWCNT) composite in the range of 20–50 °C. Faradaic efficiency of products changes with temperature and potential so that two-electron transfer product CO formation is enhanced at low potentials and temperatures while the competing hydrogen formation shows an opposite trend. Multi-electron transfer product methanol formation is more favorable at low temperatures and potentials whereas reverse applies for methane. Activity and selectivity are analyzed with DFT simulations identifying the key differences between the binding energies of CH<sub>2</sub>O and CHOH, the binding strength of CO, and the protonation of CHO intermediate. This novel experimental and theoretical understanding for CO<sub>2</sub> reduction provides insight in the influence of the various conditions on the product distribution.

## 1. Introduction

Anthropogenic CO<sub>2</sub> emissions are one of the biggest contributors to global climate change. They are mostly generated from burning fuels and as a byproduct during the production of commodity chemicals when fossil fuels are used as feedstock [1]. Globally chemical industry yields 5.5% CO<sub>2</sub> among 7.5% of the total industrial sector greenhouse gas emission [2]. To reach a sustainable future, lowering CO<sub>2</sub> emissions or reusing it as a raw material is essential. Several techniques have been suggested for lowering atmospheric CO<sub>2</sub>, e.g., sequestering, enhanced weathering, direct air capture, and biochar [3]. Besides these methods, electrochemical reduction of CO<sub>2</sub> (eCO<sub>2</sub>R) is one of the promising techniques for converting CO<sub>2</sub> waste emissions into valuable commodity chemicals and thus closing the carbon cycle and enhancing the circular economy design. By coupling an electrochemical conversion unit with environmentally friendly renewable energy sources commodity chemicals such as CH<sub>3</sub>OH, C<sub>2</sub>H<sub>5</sub>OH, and C<sub>2</sub>H<sub>4</sub> can be produced even with a

negative carbon emission footprint [1].

For the eCO<sub>2</sub>R to high-value chemicals, substantial challenges for the development of an electrocatalyst are related to selectivity, stability, and overpotential [4]. To overcome these, different electrocatalysts have been investigated including metals, metal oxides, and their derivatives. For example, metallic Cu produces a mixture of C<sub>1</sub> and C<sub>2</sub> limiting applications due to selectivity issues [5,6]. To circumvent the formation of a mixture of products, isolated metal centers coordinated with organic ligands in porphyrins, phthalocyanines, phosphines, cyclams, and polypyridine have been studied [7–12]. One of the advantages of the molecular electrocatalysts is also that their catalytic activity can be tuned by ligand design, e.g., attaching electron-withdrawing or donating groups with ligands [13–16]. In these, the coordinated metal atoms are isolated from each other and hence, behaving as single active sites with high activity and selectivity towards CO production [15,17–19]. The selectivity of these molecular catalysts has been demonstrated to depend on the experimental conditions, e.g., cobalt protoporphyrin can produce

\* Corresponding author.

E-mail address: [tanja.kallio@aalto.fi](mailto:tanja.kallio@aalto.fi) (T. Kallio).

<sup>1</sup> First two authors had equal contribution.

CO, HCOOH, CH<sub>3</sub>OH, and CH<sub>4</sub> in acidic media in a pressurized systems [20].

Cobalt phthalocyanine (CoPc) has structural differences with cobalt tetraphenyl porphyrin (CoTPP), but these two possess the same oxidation state of the central cobalt atom. The latter generates CH<sub>3</sub>OH as the main multi-electron transfer product in aqueous media upon decorating on carbon nanotube (CNT) [21,22]. Moreover, this hybrid CoPc/CNTs catalyst selectively reduces CO<sub>2</sub> to CO in aqueous media [23]. On the other hand, CoTPP has been used as a catalyst in numerous CO<sub>2</sub> electrolyzer experiments, achieving excellent conversion of CO<sub>2</sub>-to-CO in a 2 electron pathway. The state of the art for the electrocatalyst for CO<sub>2</sub> conversion to multi-electron transfer products, i.e. methane and methanol, is very limited, requiring high energy for these 6 and 8 electron transfer reactions. Hence, new approaches for producing those important chemicals at higher efficiencies and lower potentials are required to make this conversion commercially viable.

For electrocatalysts with low electrical conductivity, such as metal porphyrins, the interaction between the active material and conducting support is essential for achieving appreciable activity at low overpotentials. If a metal porphyrin is deposited on highly conductive support materials, e.g., multi-walled carbon nanotube (MWCNT), then the product formation may be tuned by an interaction between delocalized electron density of  $\pi$ -network of both metal porphyrin and MWCNT. It is noteworthy that upon the deposition of cobalt tetraphenyl porphyrine (CoTPP) on MWCNTs, the improved catalytic activity of CoTPP is attributed to easier electron transfer due to either strong  $\pi$ - $\pi$  interactions [17,18,21,22] or CH- $\pi$  interactions [24] with MWCNTs. In principle, if MWCNTs and metal porphyrin have a strong interaction, the work function decreases in comparison with their pristine moieties [25]. This promotes catalytic activity because transferring an electron from these electrodes during the potential polarization costs less energy [25].

Besides the intrinsic catalytic activities of the CoTPP/MWCNT composite, physical parameters such as temperature may influence eCO<sub>2</sub>R selectivity and reactivity. The temperature effect has been earlier investigated by T. Mizuno et al. on Sn, In, and Pb electrodes [26]. They have observed opposite temperature behavior on product distribution depending on the metal electrodes: For Sn and In, Faradic efficiency (FE) of formic acid decreased with increasing temperature. Conversely, the FE of formic acid on Pb increased with temperature [26]. Also, Hori et al. investigated eCO<sub>2</sub>R at an elevated temperature in 0.5 M KHCO<sub>3</sub> on Cu sheet electrodes and found a different trend for various products [27]. The FE of CH<sub>4</sub> decreases while the FE of C<sub>2</sub>H<sub>6</sub>, CO, and H<sub>2</sub> increase with temperature [27]. The effect of temperature on the eCO<sub>2</sub>R product formation mechanism is still unexplored. In general, temperature enhances the mass transfer [28] and the rate of the reactions in a complex manner.

Herein, an experimental and theoretical study is presented on temperature and potential effects over a CoTPP/MWCNT composite eCO<sub>2</sub>R product distribution. Notably, the effect of temperature on eCO<sub>2</sub>R on molecular catalysts has not been investigated earlier to our knowledge. To this end, a CoTPP/MWCNT composite has been synthesized and the temperature effect investigated on product formation and distribution. DFT analysis is used to explain selectivity, with the strength of \*CO binding, the CH<sub>2</sub>O bonding either through oxygen or carbon plays a major role.

## 2. Experimental methods

### 2.1. Catalyst synthesis

50 mg of MWCNTs (9 nm diameter, > 95% carbon, Nanocyl) was dispersed in 100 mL of 2 mM HCl (Merck) aqueous solution and sonicated for 1 h. 300 mg of CoTPP (dye content 85%, Sigma-Aldrich) was dispersed separately in 92 mL of 2 mM HCl solution with help of 8 mL of N,N-Dimethylformamide (DMF) (99.8%, Sigma-Aldrich) to reduce the surface tension of the aqueous solution. This dispersion was sonicated

for 1 h, too. Subsequently, these MWCNT and CoTPP dispersions were mixed and the resulting solution was sonicated again for 1 h. The mixture was magnetically stirred continuously for 48 h. During this process, a composite of CoTPP and MWCNTs was formed and precipitated at the bottom of the vial. The precipitate was separated by removing it in a small vial (40 mL in volume) and centrifuged for 1 h at 4000 rpm at 20 °C. This step was repeated three times. Each time the supernatant solution was thrown away and 2 mM HCl was added to the remnant and centrifuged again. These steps were repeated until a homogeneous colored precipitate was obtained. Finally, the precipitate was washed with Milli-Q water. Subsequently, the precipitate was solidified with liquid nitrogen (at -196 °C) and freeze-dried for 24 h. The resulting material is a CoTPP/MWCNT composite and is compared with the pristine MWCNT and CoTPP materials. Since the use of DMF is environmentally disadvantageous [29] the fabrication of the composite has been optimized to use the smallest possible amount of DMF.

### 2.2. Structural characterization

The morphology of the composite was investigated by using scanning electron microscopy (SEM) and Energy dispersive X-ray (EDX) mapping. SEM and EDX mapping was performed by JEOL JIB-4700F using EDS detector mode at different points of the surface of the composite. X-ray photoelectron spectroscopy (XPS) was performed using a Kratos Axis Ultra spectrometer with monochromated Al K $\alpha$  radiation utilizing charge neutralization, with a pass energy of 80 eV, an X-ray power of 225 W, and an analysis spot diameter of roughly 200  $\mu$ m. For survey spectra, pass energy of 160 eV was used. The binding energy scale was adjusted by setting the C 1s peak related to CoTPP to 284.8 eV.

Interaction between CoTPP and MWCNTs and the composition of the composite was further investigated by measuring Raman spectra using JY Lab Ram300 configured with a helium-neon laser of 633 nm. Also, thermogravimetric analysis was performed with a TGA Q500 (TA instrument) at 5 °C/min temperature up to 800 °C in presence of air.

### 2.3. Cyclic voltammetry

The electrochemical characterization of all prepared electrodes was carried out in a one-compartment three-electrode rotating disk electrode (RDE) system (Pine Research Instrument, USA) at room temperature in N<sub>2</sub> and CO<sub>2</sub> (99.99%, AGA) environments. Before the measurements, all the glassware was cleaned with 0.5 M KMnO<sub>4</sub> and ultrapure water (18.2 M $\Omega$  cm). The catalyst was loaded on a 5 mm diameter glassy carbon electrode (GCE) used as a working electrode (WE). Before catalyst loading, GCE was polished with 0.3  $\mu$ m and 0.05  $\mu$ m alumina slurry on a microporous cloth. Then it was repeatedly rinsed with ultrapure water, sonicate in ethanol-water, and rinsed again with water. An Ir wire and a commercial Ag/AgCl (saturated) electrode placed in a Luggin capillary were used as a counter electrode (CE) and a reference electrode (RE), respectively. Potential is converted to a reversible hydrogen electrode (RHE) using the equation

$$E_{\text{RHE}} = E_{\text{Ag/AgCl}} + 0.199V + \frac{2.303RT}{nF} \text{pH} \quad (1)$$

where  $R$  is the universal gas constant,  $T$  is the temperature,  $F$  is the Faraday constant and  $n$  is the number of electrons. In the temperature range of 20–50 °C potential variation of the reference electrode was less than 20 mV and hence it is ignored from the calculation. The potential was represented without  $iR$  correction.

For the RDE measurements, the composite ink was prepared by dispersing a calculated amount of the composite in pure ethanol and sonicate for 5–10 min. From this composite ink, ca. 0.28 mg/cm<sup>2</sup> was drop casted on the GCE and then 5  $\mu$ L of diluted 5 wt% Nafion solution (Sigma-Aldrich) was poured on the catalyst layer and let to dry overnight. The 0.1 M KHCO<sub>3</sub> (ACS reagent, 99.7%, Sigma-Aldrich)

electrolyte was prepared by using ultrapure water (18.2 MΩ cm) and 120 mL electrolyte solution was taken in the three-electrode electrochemical cell. A Luggin capillary was used to set the RE position and to minimize the  $iR$  losses between the WE and RE. Before measurements, N<sub>2</sub> gas was bubbled for 30–45 min to remove dissolved oxygen. In the RDE system, the maximum rotation rate (2500 rpm) was used to avoid the sticking of gas bubbles on the electrode surface. In this N<sub>2</sub> atmosphere, a stable cyclic voltammogram with a scan rate of 20 mV/s was recorded as a reference for the hydrogen evolution reaction (HER). After that, CO<sub>2</sub> gas was bubbled for 30–40 min in the electrolyte. A pH of the electrolyte was measured before and after CO<sub>2</sub> bubbling, and it was observed that CO<sub>2</sub> bubbling decrease the pH of the electrolyte from 8.80 to 6.80. A stable cyclic voltammogram with a scan rate of 20 mV/s was recorded in the CO<sub>2</sub> saturated solution, to observe the onset of the CO<sub>2</sub> reduction reaction. N<sub>2</sub> and CO<sub>2</sub> were continuously bubbled above the electrolyte during the CV experiments.

## 2.4. Chronoamperometry and product analysis

To elucidate the reaction products, controlled potential electrolysis (Iviumstat.XRi, Ivium technologies) was performed in a thermostat two-compartment H-type glass cell. For that purpose, the catalyst ink was sprayed on a 12.56 cm<sup>2</sup> one-sided microporous gas diffusion layer (GDL-CT series, FuelCellsEtc) and used as a WE. A large-sized Pt mesh and a commercial Ag/AgCl (saturated) electrode were used as a CE and RE, respectively. The compartments were separated with a pretreated Nafion 115 membrane and each compartment was filled with 80 mL of 0.1 M KHCO<sub>3</sub> electrolyte. During the electrochemical tests, the temperature of the cell was controlled to a constant value by a water bath. Before the electrolysis, N<sub>2</sub> gas was bubbled in 0.1 M KHCO<sub>3</sub> electrolyte for 30–40 min to remove dissolved oxygen. Then, CO<sub>2</sub> was bubbled for 30–40 min to saturate the electrolyte. Before and after the saturation with CO<sub>2</sub>, the pH of the electrolyte was measured with a pH meter at each studied temperature (i.e. 20 °C, 30 °C, 40 °C, and 50 °C). Before performing bulk electrolysis at  $-0.60 V_{RHE}$ ,  $-0.80 V_{RHE}$ , and  $-1.00 V_{RHE}$  at the selected temperatures, a stable CV at 50 mV/s was obtained in both N<sub>2</sub> and CO<sub>2</sub> atmosphere. It is noteworthy that during the bulk electrolysis, CO<sub>2</sub> was continuously bubbled in the WE compartment to provide a constant CO<sub>2</sub> supply. The electrolyte in the WE and CE compartment was stirred continuously to favor the mass transport during the bulk electrolysis. The identification of intermediates for the CH<sub>3</sub>OH and CH<sub>4</sub> formation is substantial to understand the mechanism. Therefore, bulk electrolysis starting by 0.01 M HCHO and HCOOH were performed at  $-0.60 V_{RHE}$  at 30 °C and  $-1.00 V_{RHE}$  at 30 °C and 50 °C. Furthermore, to understand the adsorption of CO on the active site of the composite, CO electrolysis was performed at  $-1.0 V_{RHE}$  in 20 °C and 50 °C by employing flow cell system because of its very low solubility in aqueous solution. At the end of 2 h CO electrolysis, catholyte was analyzed with HPLC and mass spectrometry (MS).

To analyze the gas products, the electrochemical H-type cell was directly connected with an Agilent 6890 N series three-way valve gas chromatograph (GC) equipped with flame ionization (FID) and thermal conductivity (TCD) detectors. The FID was used to detect hydrocarbons e.g., CH<sub>4</sub>, whereas the TCD was used to detect permanent gases like H<sub>2</sub>, CO, and CO<sub>2</sub>. Gas samples from the headspace during the electrolysis were analyzed every 30 min using a sampling volume of 0.25 mL. Calibration standards were analyzed before the measurements. CO<sub>2</sub> was bubbled during the bulk electrolysis at a flow rate of 20–22 mL/min. The FE of gaseous products was determined by using the following adapted formula [30].

$$FE = \frac{n_p n_i F}{It} \times 100\% \quad (2)$$

where,  $n_p$  is the number of moles of gas products,  $n_i$  is the number of

electrons required for that product,  $F$  is the Faraday constant,  $I$  is the current during sampling time  $t$ . The number of moles of a gaseous product,  $n_p$ , was calculated by using the following formula.

$$n_p = \frac{PVX_p}{RT} \quad (3)$$

where  $V$  is the sample loop volume of the GC,  $P$  is the atmospheric pressure,  $R$  is the universal gas constant,  $T$  is the temperature and  $X_p$  is the mole fraction of the gas product obtained from the GC.

The liquid products were analyzed with a high-performance liquid chromatograph (HPLC, Water Alliance, 2690) coupled with an Aminex HPX-87H (Bio-Rad) column for product separation. CH<sub>3</sub>OH is not UV sensitive and so a refractive index (RI, Water Alliance) detector was used. A 5 mM H<sub>2</sub>SO<sub>4</sub> acid solution was used as eluent with a flow rate of 0.6 mL/min. The temperature of the column was maintained at 65 °C during the measurement. The products were quantified comparing with standard solutions of formic acid and methanol. Faradaic efficiency (FE) of liquid products was determined by using the following formula:

$$FE = \frac{n_i}{\int_0^t Idt} \times \frac{c_i F V}{100\%} \quad (4)$$

where  $n_i$  is the number of electrons required to produce the  $i_{th}$  product,  $c_i$  is the concentration of that product obtained from the HPLC analysis,  $V$  is the volume of the electrolyte in the electrolysis cell,  $I$  is the average current during bulk electrolysis.

Turn over frequency (TOF) calculation was performed by using the following formula:

$$TOF = \frac{Q * FE}{nF} \bigg/ \frac{m_w * w\%}{M_w * t} \quad (5)$$

where  $Q$  is the total charge during chronoamperometry,  $FE$  is the Faradaic efficiency,  $F$  is Faraday constant,  $n$  is the number of electrons exchanged for the product formation,  $m_w$  is the loading of the composite on gas diffusion electrode,  $w\%$  is the weight-% of catalyst (e.g., Co for CoTPP) from XPS,  $M_w$  molecular weight of catalyst,  $t$  is for time used to express the TOF unit.

## 2.5. Computational details

Spin-polarized Density Functional Theory (DFT) as implemented in the Vienna Ab initio Simulation Package (VASP)[31,32] was used with the GGA functional PBE-D3 [33,34]. The core electrons were described by projector augmented wave (PAW) [31,35] while valence electrons were expanded in plane waves with a kinetic energy cut-off at 500 eV. The molecular catalysts (CoTPP/MWCNT and CoPc/CNT) were constructed on a graphene layer expanded in a (9 × 9) supercell, while FeN<sub>4</sub>C catalyst is represented with a two-dimensional graphene layer with (6 × 6) supercell replacing 4 carbon atoms by 4 nitrogen atoms. These layers were interleaved by 18 Å and 12 Å vacuum along the z-direction for molecular and FeN<sub>4</sub>C catalyst, respectively. The Brillouin zone was sampled using a 2 × 2 × 1  $k$ -point for molecular catalyst and 3 × 3 × 1  $k$ -point for FeN<sub>4</sub>C mesh generated with the Monkhorst-Pack method [36], where structures were relaxed with a force threshold of 0.05 eV/Å. The computational hydrogen electrode (CHE) method [37, 38] was used to calculate the Gibbs free energy ( $\Delta G$ ) of each electron transfer step in the electrochemical CO<sub>2</sub> reduction (eCO<sub>2</sub>R) and hydrogen evolution reaction (HER). Details on thermodynamic corrections are discussed in the section of Calculation details in the [Supporting Information](#). The optimized structures can be retrieved from the open access database ioChem-BD [39,40].



### 3. Results and discussion

#### 3.1. Structural characterization of CoTPP/MWCNT

The CoTPP/MWCNT composite morphology was characterized by scanning electron microscopy (SEM). In Fig. 1a the SEM morphological image of the composite is presented, where dispersion of CoTPP on MWCNT is observed. In addition, energy dispersive x-ray (EDX) was used to investigate elemental composition, where Fig. 1a depicts a homogeneous distribution of C, N, and Co. CoTPP is in a planar configuration: When deposited on the nanotube, phenyl groups are in perpendicular configuration, where hydrogen atoms of the aromatic phenyl rings interact with the  $\pi$  electron system of MWCNT forming multiple CH- $\pi$  interactions [41–43] (see Fig. 1b). Each of the four phenyl aromatic rings forms two CH- $\pi$  interactions, where the H...C distances extend from 2.65 Å to 3.33 Å (see Fig. S1).

In order to benchmark experimental findings over the CoTPP/MWCNT composite, CoPc/CNT (Fig. S2) and FeN<sub>4</sub>C (Fig. S3) catalysts were modeled. A CoPc/CNT catalyst generates CH<sub>3</sub>OH as the main multi-electron transfer product in aqueous media [19] while the FeN<sub>4</sub>C is producing CH<sub>4</sub> [44]. A CoPc complex is in a square planar configuration. Structural features such as secondary coordination sphere of nitrogen atoms, and planar phenyl rings, which interact with the  $\pi$  system of CNT forming multiple  $\pi$ - $\pi$  interactions, makes a CoPc complex stable. Interaction between both  $\pi$  systems is around 3.5 Å, adsorption energies of clean CoTPP and the CoPc complexes on the graphene layer are -1.94 eV and -2.28 eV, respectively.

Raman spectroscopy was employed for further characterization of the composite (Fig. 1c). The Raman spectrum of MWCNT exhibits two characteristic peaks: The D-band (ca. 1314 cm<sup>-1</sup>) is assigned to the sp<sup>3</sup> hybridized carbon or the disordered nanotube structure/edge plane [45, 46] and the G-band (ca. 1575 cm<sup>-1</sup>) correspond to the sp<sup>2</sup> hybridized carbon atoms from basal plane which are generated by tangential vibrational mode of the nanotubes. The CoTPP peaks in a range of 300–1600 cm<sup>-1</sup> are visible and originate from the symmetric and asymmetric stretching and bending molecular vibrational modes of chemical species [47]. The composite spectrum shows contribution from both components. The most intense peaks of CoTPP are well observed

while the D and G bands originating from MWCNT are observed as a hump at ca. 1300 and 1600 cm<sup>-1</sup>.

The oxidation state of Co was investigated with XPS. The Co 2p XPS spectra (Fig. 1d) of CoTPP and the CoTPP/MWCNT composite both show a Co 2p<sub>3/2</sub> peak at binding energy 780.3 eV. This value and the spectral shape are typical for the 2+ oxidation state also found in CoTPP molecular multilayers [48,49]. For CoTPP monolayers on metallic substrates even 2 eV shifts of the Co 2p peaks to lower binding energy have been observed indicating direct electronic interaction with the substrate [50]. However, in this case, no shift is observed in the Co 2p peaks suggesting that the possible interaction is not via the central cobalt ion. This is further in agreement with the DFT results based on the magnetization found,  $\mu_B = 1$  (Table S5 and Fig. S4).

In Fig. 1e the thermogravimetric analysis is performed to investigate the amount of Co in the composite. The pristine MWCNT decomposes at 650 °C whereas the CoTPP/MWCNT composite and pristine CoTPP complex degrade at a lower temperature of 350 °C. Hence, it appears that CoTPP enhances MWCNT decomposition suggesting again strong interaction between MWCNT and CoTPP in the composite. Based on these TGA measurements, the residual amount of cobalt is 8.47 wt% in the composite which is slightly lower than the theoretical amount of 8.77 wt% in CoTPP. Furthermore, the elemental Co content of the composite quantified from XPS signals is 4.7 wt% (Table S6).

#### 3.2. Catalytic performance of CoTPP/MWCNT

The electrochemical window of catalytic activity was first screened in the RDE setup recording CVs at room temperature for pristine MWCNT, CoTPP, and the composite. With the 6:1 ratio of CoTPP to MWCNTs, the latter provides the highest current density in CO<sub>2</sub>-saturated 0.1 M KHCO<sub>3</sub>, while pristine CoTPP and MWCNT exhibit hindered activity at this condition as indicated by lower currents and shifting of the onset potentials to more negative values (Fig. 2a). Among different composite compositions, 6:1 CoTPP/MWCNTs appears to be optimal for promoting eCO<sub>2</sub>R as indicated by higher currents obtained in the potential range of -0.5 – (-1.2) V<sub>RHE</sub> in the CO<sub>2</sub> saturated electrolyte compared to the N<sub>2</sub> saturated one (Fig. 2a and b). This is attributed to an appropriate balance between the eCO<sub>2</sub>R promoting CoTPP centers and

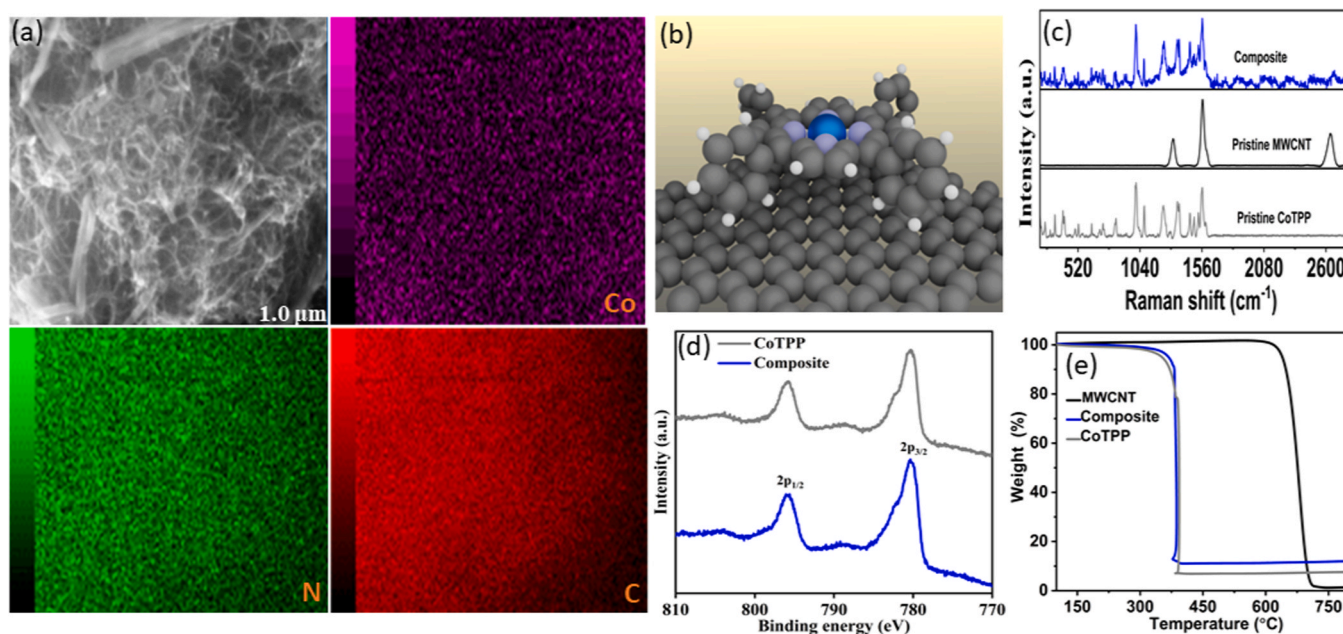


**Fig. 1.** The CoTPP/MWCNT composite structural characterization. (a) Morphological SEM image and EDX elemental mapping of Co (purple), N (green), and C (red). (b) Optimized structural computational model, where C is in gray, N in purple, Co in blue, and H in white. (c) Raman spectra, (d) Co 2p XPS spectra, and (e) TGA curves.

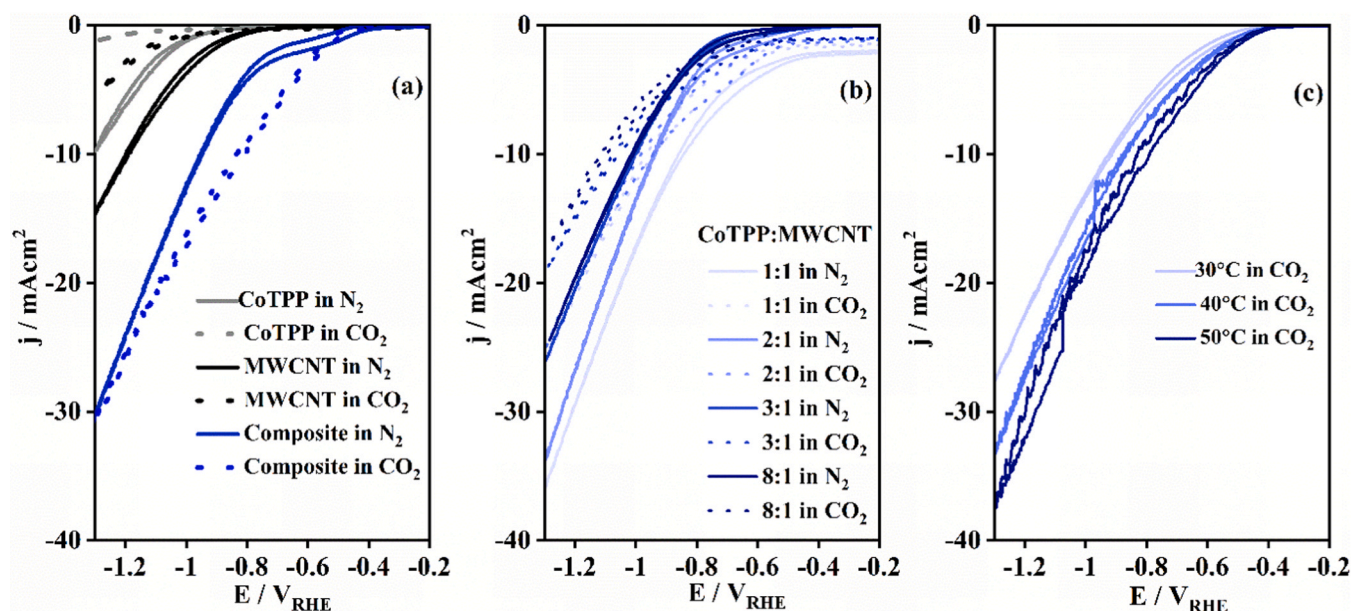


**Fig. 2.** Cyclic voltammograms (a) over pristine MWCNT, CoTPP, and CoTPP/MWCNT (6:1 ratio), (b) for different CoTPP:MWCNT load ratios (1:1, 2:1, 3:1, 8:1) at room temperature in the  $N_2$  (pH 8.8) and  $CO_2$  (pH 6.8) saturated 0.1 M  $KHCO_3$  electrolyte and (c) CV curves for the CoTPP/MWCNT composite at 30 °C, 40 °C, and 50 °C in  $CO_2$  saturated 0.1 M  $KHCO_3$ . The scan rate was 20 mV/s and progressed first to the cathodic direction. All the potentials are presented here without iR correction.

the electron delivering MWCNTs when having this particular composition. Below results for the optimal 6:1 CoTPP/MWCNTs are reported and discussed.

The onset potentials for CoTPP and MWCNT are ca.  $-0.8$ , and  $-0.9$   $V_{RHE}$ , respectively, in  $N_2$  environment. At  $-1.30$   $V_{RHE}$ , current density reaches  $-14.5$   $mA/cm^2$  for MWCNT and  $-10$   $mA/cm^2$  for CoTPP indicating activity for water reduction and formation of  $H_2$  [51]. In the  $CO_2$  saturated electrolyte, the onset potentials are more negative for both pristine MWCNT and CoTPP in comparison to  $N_2$  saturated environment indicating that neither of these samples is particularly active towards reducing  $CO_2$ . For the composite in the  $N_2$  purged electrolyte, a shoulder before the linear current increase region is visible. The onset is at ca.  $-0.50$   $V_{RHE}$ , close to  $Co^{2+}/Co^+$  transformation associated with proton reduction [52], whereas the linear increase is observable at ca.  $-0.80$   $V_{RHE}$  and ascribed to the direct water reduction [51]. Hence, the first plateau and subsequent linear current increase are suggested to correspond to the direct proton and water reduction, respectively. While in  $CO_2$  rich media, the onset potential does not change notably but the current density increase is steeper and featured by the absence of the wave indicating a change in the reaction mechanism.

To elucidate the direct proton and  $H_2O$  reduction mechanism, CV experiments were performed at 30 °C, 40 °C, and 50 °C in the  $N_2$  and  $CO_2$  saturated electrolytes. The change in the water reduction mechanism in  $N_2$  is seen in Fig. S6 where at 30 °C the current characteristics is similar to the room temperature behavior (Fig. 2a). However, at 40 °C and 50 °C (Fig. S6)  $H_2O$  reduction becomes predominant. In the  $CO_2$  saturated electrolyte (Fig. 2c), no shoulder is seen at the studied temperatures and reduction current continuously increases in the measured potential range though concomitant cobalt reduction ( $Co^{2+}$  to  $Co^+$  and  $Co^+$  to  $Co^0$ ) can take place [53, 54]. On the other hand, on the electrode surface,  $CO_2$  encounters the polarized electrode. As  $CO_2$  molecules have high negative electron affinity [55], they can only accept electrons from  $Co^+$  and transform it to  $Co^{2+}$  during to the negative potential direction going forward sweep. The electrochemical activity of composite with different loading of CoTPP on MWCNT was investigated. Fig. 2b shows the CVs of varying loading of CoTPP on MWCNT. At 1:1 ratio in  $N_2$  environment, composite is quite active for HER which is evident from

large current density from forward going CV sweep. Ratios 2:1 and 3:1 shows different activity from  $-0.55$   $V_{RHE}$  to ca.  $-0.95$   $V_{RHE}$ . Within this potential range, HER is suppressed in  $CO_2$  environment. Conversely, the composite with 8:1 ratio is losing activity in this potential range which indicates that exceeding the ratio of 6:1 will decrease the activity of composite. The reason may be that the CoTPP mostly covers the MWCNT surface which impedes electron delivery and thus deteriorates the conductivity.

To analyze product distributions of simultaneous electrocatalytic reduction of  $CO_2$ ,  $H_2O$ , and subsequent reduction of the intermediate product CO (detailed discussion below in Section 3.5) chronoamperometric (CA) electrolysis in the H-cell were conducted (Fig. 3). The GC detected  $H_2$  and CO, and at high temperatures also  $CH_4$ , as gaseous products. At the end of the constant potential electrolysis (Fig. 3), the catholyte was collected and analyzed with the HPLC. In these measurements,  $HCOO^-$  and  $CH_3OH$  were detected as liquid products.  $HCOO^-$  is generated with a low Faradaic efficiency, and partial current density.

In Fig. 4(a–c) the relative fraction of all products formed during the CA on the CoTPP/MWCNT composite is presented while the partial current densities are depicted in Fig. 4(d–f). Generally, partial current densities reveal the average amounts of products generated in a certain duration. Current densities obtained at  $-0.60$   $V_{RHE}$ ,  $-0.80$   $V_{RHE}$ , and  $-1.00$   $V_{RHE}$  at selected temperatures, show no indication of deactivation within the 4 h measurement period (Fig. 3). No morphological changes could be observed after these experiments when comparing the pristine and used electrodes structures and composition with SEM imaging and EDX elemental mapping (Figs. 1a and S5) suggesting that the CoTPP/MWCNT composite is stable during these measurements.

The intrinsic activity of catalysts is revealed by the turnover frequency (TOF) values. The TOF values for methanol formation reach ca.  $0.02$   $s^{-1}$  at  $-1.0$   $V_{RHE}$  at 50 °C while for CO formation they reach ca.  $0.06$   $s^{-1}$  at 20 °C in the same potential (see Fig. S12). Thus, the composite shows different trend of activity in terms of potential and temperature for CO and  $CH_3OH$  formation.

### 3.3. Temperature and potential influence on the product distribution

Regarding the selectivity in terms of faradaic efficiencies (FE), two



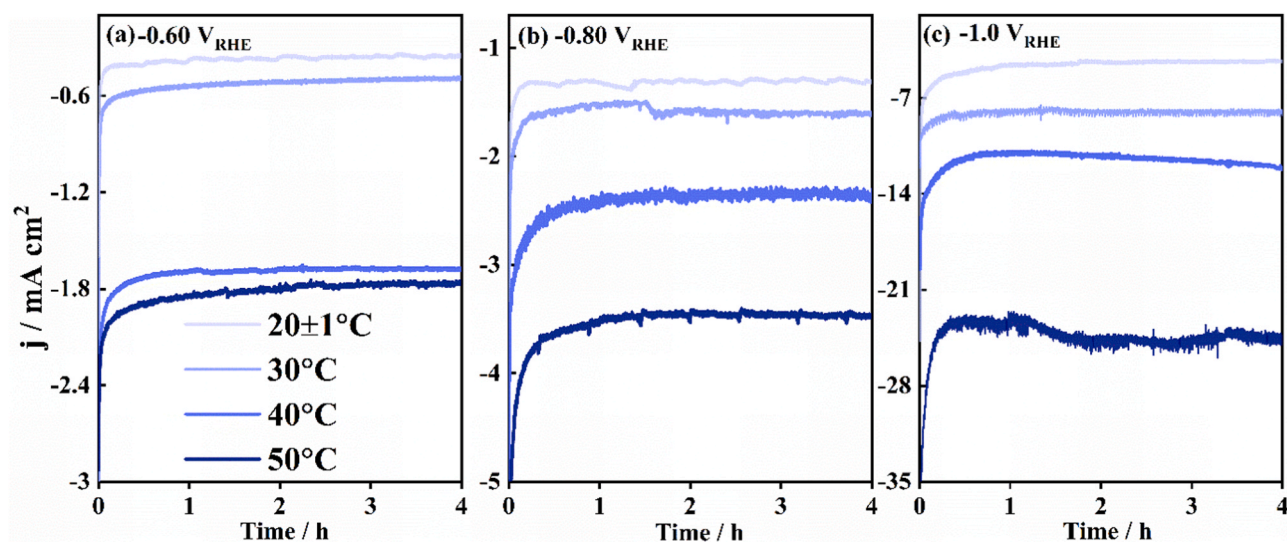


Fig. 3. Constant potential electrolysis over CoTPP/MWCNT at (a)  $-0.6 \text{ V}_{\text{RHE}}$ , (b)  $-0.8 \text{ V}_{\text{RHE}}$ , and (c)  $-1.0 \text{ V}_{\text{RHE}}$ . The data was obtained by chronoamperometry (CA) for 4 h, performed in the  $\text{CO}_2$  saturated  $0.1 \text{ M KHCO}_3$  aqueous electrolyte.

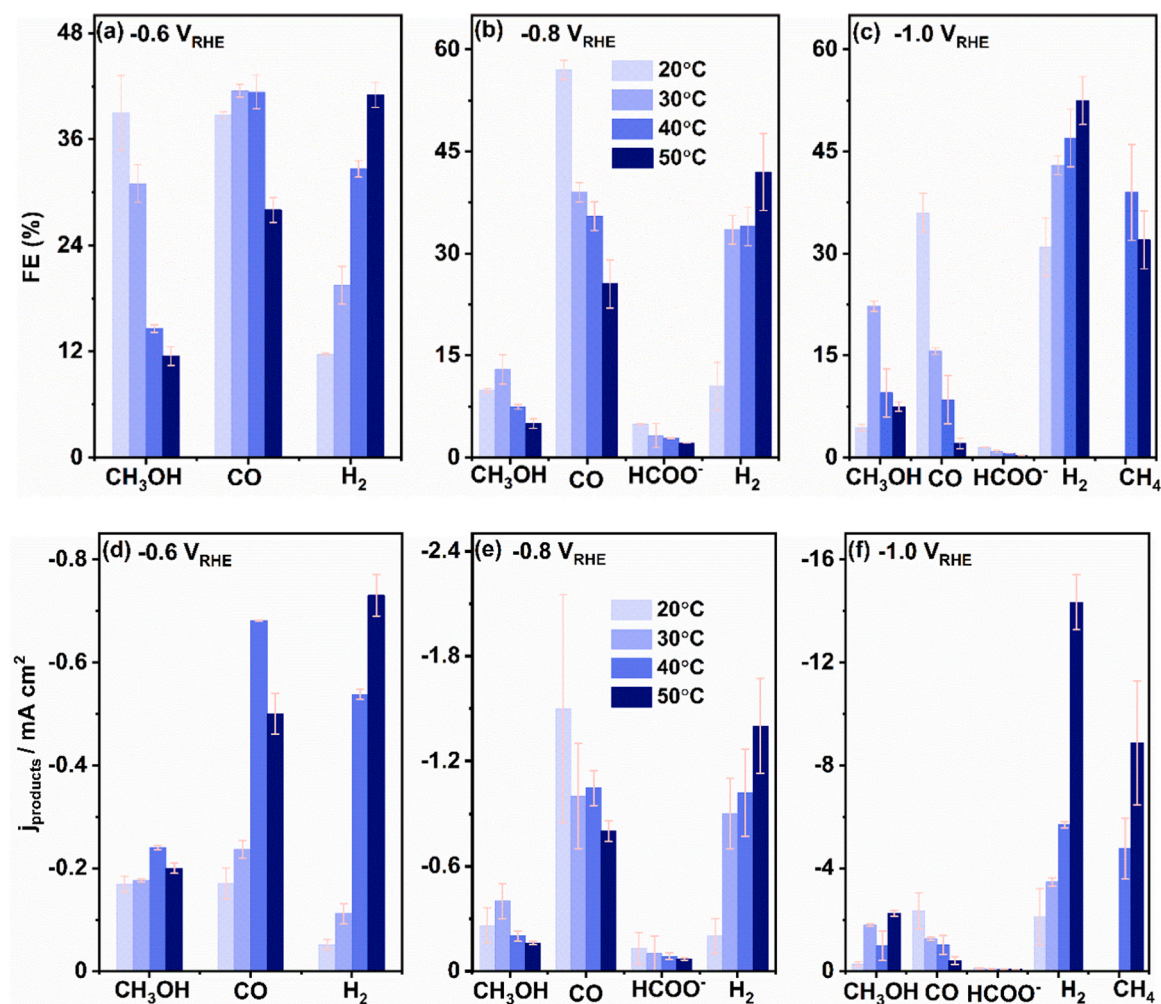


Fig. 4. Product analysis over CoTPP/MWCNT. (a, b, c) Faradaic efficiency with error bars and (d, e, f) partial current density with error bars of all the detected products at studied temperatures where (a, d)  $-0.6 \text{ V}_{\text{RHE}}$ , (b, e)  $-0.8 \text{ V}_{\text{RHE}}$ , and (c, f)  $-1.0 \text{ V}_{\text{RHE}}$ .

trends in the product distribution influenced by the temperature are noticed (Fig. 4). With increasing temperature, the formation of  $\text{H}_2$  is increasing, while for  $\text{CH}_3\text{OH}$ ,  $\text{HCOO}^-$  and  $\text{CO}$  the opposite trend is observed. Moreover,  $\text{CH}_4$  appears only at the highest investigated temperatures and potential.

For the formation of  $\text{H}_2$ , the parallel increase of FE and partial current densities can be seen with temperature and potential (see Fig. 4). Indeed, the increasing temperature appears to favor the  $\text{H}_2\text{O}$  reduction as the FE of  $\text{H}_2$  at elevated temperature is more than 40% at  $-0.6 \text{ V}_{\text{RHE}}$ , while at  $-1.0 \text{ V}_{\text{RHE}}$  it increases even closer to 60% at  $50^\circ\text{C}$ . Hence, a large contribution to the current generation comes from the direct reduction of  $\text{H}^+$  and/or  $\text{H}_2\text{O}$  to  $\text{H}_2$  (see also Fig. S6) while the formation of  $\text{CO}$  with increasing temperature decreases. The highest  $\text{CO}$  selectivity of 57% is observed at  $-0.8 \text{ V}_{\text{RHE}}$  at the  $20^\circ\text{C}$  temperature. Syn-gas can be produced at  $30^\circ\text{C}$  and higher temperatures at  $-0.8 \text{ V}_{\text{RHE}}$ , where the ratios of  $\text{CO}$  and  $\text{H}_2$  are close to 1:1. At  $-0.6 \text{ V}_{\text{RHE}}$  formation of  $\text{CO}$  dominates, excluding the highest temperature. The temperature influence could be a method to control components ratios for the formation of the syn-gas. For metgas synthesis, for example, the ratio of  $\text{CO}$  and  $\text{H}_2$  are accommodated to 1:2 to enhance the  $\text{CH}_3\text{OH}$  synthesis [56].

At  $20^\circ\text{C}$  and  $-0.6 \text{ V}_{\text{RHE}}$  the main product is  $\text{CH}_3\text{OH}$ , while at the same potential production of  $\text{CH}_3\text{OH}$  is decreasing with increasing temperature. The  $\text{eCO}_2\text{R}$  proceeds so that adsorbed  $\text{CO}_2$  reduces via parallel pathways to liquid six electron transfer and gaseous two electron transfer products  $\text{CH}_3\text{OH}$  and  $\text{CO}$ , respectively. Therefore, a considerable amount of  $\text{CO}$  is desorbed from the electrocatalyst surface before further reduction and it is suggested to be an intermediate species during the formation of  $\text{CH}_3\text{OH}$ .

Interestingly, the formation of  $\text{C}_1$  product  $\text{CH}_4$  at  $-1.0 \text{ V}_{\text{RHE}}$  is observed only at elevated temperatures  $40^\circ\text{C}$  and  $50^\circ\text{C}$ . Under those conditions, selectivity based on FE is more than 35%. To generate the

above-described products, upon adsorption and reduction of  $\text{CO}_2$ , the first main intermediate is  $^*\text{CO}$  (Fig. 5a) from which  $\text{C}_1$  products can be obtained. Releasing  $\text{CO}$  would regenerate the catalyst; otherwise,  $^*\text{CO}$  can further hydrogenate to  $^*\text{CHO}$ .  $^*\text{CHO}$  can be further reduced by following two pathways: forming (i)  $^*\text{OCH}_2$  by breaking a  $\text{Co}-\text{C}$  bond and forming a  $\text{Co}-\text{O}$  and  $\text{C}-\text{H}$  bond, which can either desorb or continue to react eventually forming  $\text{CH}_3\text{OH}$  (Fig. 5b); or (ii)  $^*\text{CHOH}$  by protonation of  $\text{O}$  atom, which can evolve to  $\text{CH}_3\text{OH}$  (two proton and electron transfers) or  $\text{CH}_4$  and  $\text{H}_2\text{O}$  (four proton and electron transfers) depending on the hydrogenation pathway (Fig. 5c). Alternatively, the initial  $^*\text{CO}$  could also hydrogenate to  $^*\text{COH}$  (Fig. 5d). Additional hydrogenation with concomitant water elimination could produce  $^*\text{C}$ [57]. This intermediate can accept up to four protons and electrons to finally yield  $\text{CH}_4$ . This mechanism is not chemically possible for single-atom metals as carbon needs to form four bonds.

### 3.4. Understanding the product selectivity

There are approaches to understand product selectivity based on the DFT results. The First would be to determine  $\text{CO}$  binding energy, to establish if  $\text{CO}$  can be released or reduced towards  $\text{C}_1$  products. To identify a selectivity descriptor between  $\text{CH}_4$  and  $\text{CH}_3\text{OH}$  the oxophilicity of the catalyst is determined, which correlates with the binding energy of  $\text{O}$  [58]. This descriptor has been employed to understand trends over transition metals:  $\text{CH}_3\text{OH}$  has been detected on the poorly oxophilic  $\text{Au}$  metal surface, while  $\text{CH}_4$  is found for the strongly oxophilic  $\text{Fe}$ .

To benchmark this approach, this theory is applied here for  $\text{CoTPP}/\text{MWCNT}$  and a reference  $\text{FeN}_4\text{C}$  catalyst. The binding energy of  $^*\text{O}$  for  $\text{CoTPP}/\text{MWCNT}$  is  $-2.65 \text{ eV}$ , while for the  $\text{FeN}_4\text{C}$  value is  $1.18 \text{ eV}$  more exothermic. Indeed, on  $\text{FeN}_4\text{C}$  active sites,  $\text{CH}_4$  has been detected [44]

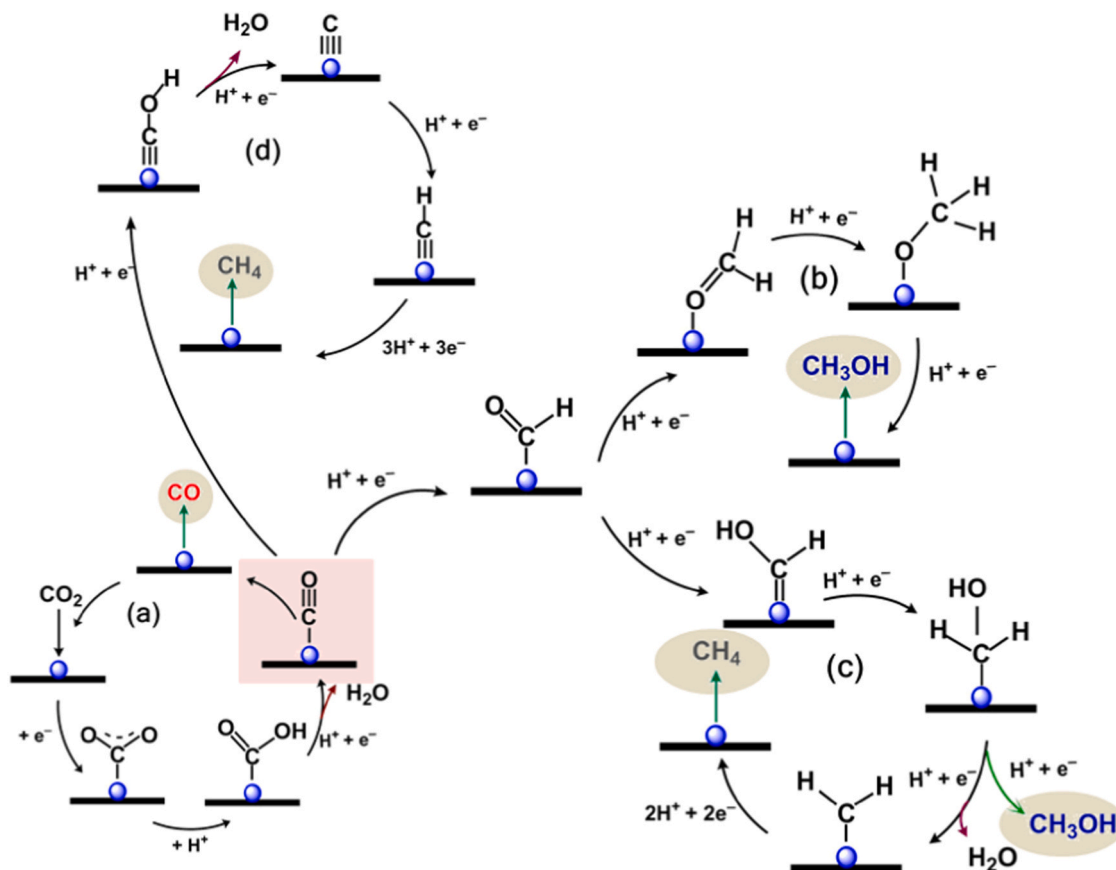


Fig. 5. Electrochemical  $\text{CO}_2$  reduction network. Reaction mechanism towards (a)  $\text{CO}$ , (b)  $\text{CH}_3\text{OH}$ , (c)  $\text{CH}_4$  and side product  $\text{CH}_3\text{OH}$ , and (d)  $\text{CH}_4$  on  $\text{CoTPP}/\text{MWCNT}$ .



thus reinforcing the practical use of the descriptor. In addition, the selectivity of  $C_1$  product can correspond to the relative energy of oxygen  $^*OCH_2$  or carbon bound  $^*CHOH$  intermediates. Based on the DFT mechanism,  $CH_2O$  can either be reduced to the oxygen bonding species  $^*OCH_3$ , which yield alcohols, or the carbon bonding  $^*CH_2OH$  intermediate that is the precursor of fully reduced hydrocarbons [59]. However, the difference in selectivity in the studied case can also be identified by comparing  $^*OCH_2$  and  $^*CHOH$  intermediates. For CoTPP/MWCNT and CoPc/CNT,  $^*OCH_2$  binding energy is more exothermic than  $^*CHOH$ , while for  $FeN_4C$  the opposite trend is observed (see Table S9). Furthermore, the electrochemical activity and selectivity are analyzed by calculating the binding energies of the possible intermediates. For CoTPP/MWCNT, the Co-O intermediate binding is exothermic  $-1.21$  eV, while the binding of Co-C is  $-0.04$  eV at  $-0.6$  V<sub>RHE</sub>, which means the production of  $CH_3OH$  is favorable. For comparison, the binding energy of Fe-C is  $-0.66$  eV and  $-0.38$  eV for Fe-O, and in that case,  $CH_4$  is formed.

To compare investigated product formation pathway, electrolysis of formic acid ( $HCOOH$ ) and formaldehyde ( $CH_2O$ ) was performed at  $-0.60$  V<sub>RHE</sub> at  $30$  °C and  $-1.00$  V<sub>RHE</sub> at  $30$  °C and  $50$  °C. Interestingly,  $HCOOH$  electrolysis produces  $H_2$ , while  $CH_2O$  produces both  $CH_3OH$  and  $CH_4$ . The free energy network for the different product pathways is presented in Fig. 7.

Compared to previous results in the literature, at room temperature different Co complexes (see Table S10) predominately produce CO, except the CoPc/CNT [23] catalyst which has been found to also produce  $CH_3OH$ . When the same complex has been used but supported on a single-walled nanotube, CoTPP/CNT [60] up to 90% FE of CO production at  $-0.68$  V<sub>RHE</sub> has been observed (see Fig. S11). In contrast, in this study at  $20$  °C temperature and  $-0.6$  V<sub>RHE</sub>, the production of  $CH_3OH$  is observed. From simulations presented here, the binding of  $^*CO$  is the determining intermediate to produce higher-value products and in Fig. 7b the pathway towards CO is shown at  $-0.8$  V<sub>RHE</sub>. Fig. S10 shows that CoTPP/MWCNT binds CO weaker (by  $0.95$  eV) than  $FeN_4C$  does. Hence, the binding strength of CO can be understood to trigger the product selectivity towards hydrocarbons or alcohols. As Fe in the  $FeN_4C$  catalyst binds CO strongly, therefore, it produces  $CH_4$ .

At the lower potential region, CO desorption is accelerated by higher

temperature as indicated by the increase of its partial current density ( $j_{CO}$ ) with the temperature [61,62]. The protonation of  $^*CO$  to  $^*CHO$  is exothermic for the composite, which makes CO easier to protonate towards  $CH_3OH$ . According to the DFT at  $-0.8$  V<sub>RHE</sub>, the binding energy of  $^*CO$  is more exergonic, which means that CO desorption is less favorable. The reason for a difference in the experimental and DFT results may be due to local pH change. At higher potentials, the pH change in the electrode/electrolyte interface is pronounced because of the higher reaction rates [51,63,64].

The adsorption of  $^*CO$  and its further reduction to  $CH_3OH$  can be experimentally investigated by CO electrolysis on the composite. This was performed in a flow cell configuration to avoid mass transfer limitations present in an H-cell due to very low solubility of CO, and products were analyzed with a mass spectrometer. Fig. 6 shows that all the peaks related to mass fragments of  $CH_3OH$  increase from a stable background and this is confirmed by the calibration with a standard  $CH_3OH$  solution (Fig. S14). Thus, this indicates that CO is adsorbed on the active site of the composite and further reduced to  $CH_3OH$ .

In order to explain the observed trend, the CoPc/CNT activity is introduced. The influence of structural features of catalytic sites, meaning the number of coordinated N atoms, and configuration of phenyl groups, play an important role in the performance during the reaction. The results for  $CO_2$  reduction obtained over the CoPc/CNT catalyst [23] show that at  $-0.82$  V<sub>RHE</sub> around 80% of CO is produced, and at  $-0.94$  V<sub>RHE</sub> around 44% of  $CH_3OH$  is formed (see Fig. S11). Fig. S13 presents Gibbs free energy diagram for the CoTPP/MWCNT and CoPc/CNT molecular catalysts at  $-0.6$  V<sub>RHE</sub>. Comparing  $^*CO$  binding energies between two systems, a difference of  $1.71$  eV is observed. CoTPP/MWCNT binds CO stronger than CoPc/CNT and this yields production of  $CH_3OH$  at  $-0.6$  V<sub>RHE</sub>. According to the weak binding energy of the  $^*CO$  intermediate for CoPc/CNT at  $-0.8$  V<sub>RHE</sub> potential, CO is desorbed rather than reduced further to produce  $CH_3OH$  (see Fig. S13). In Fig. 7a, the pathways towards forming  $CH_3OH$  are presented. As the oxygen bonding of  $CH_2O$  is more favorable, the reduction will continue through  $^*OCH_2$  and  $^*OCH_3$  intermediate.

In the case of  $CH_4$  formation (Fig. 5d), it can proceed through the  $^*COH$  or  $^*CHO$  intermediate, where the former is higher in energy by  $1.94$  eV. Therefore, it is excluded as a possible pathway. As  $CH_4$  is traced

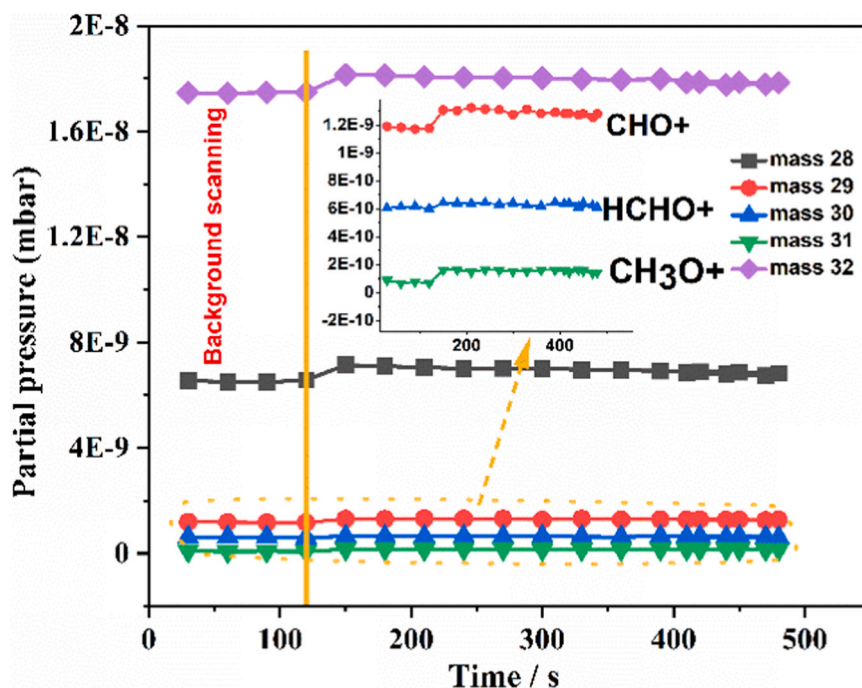
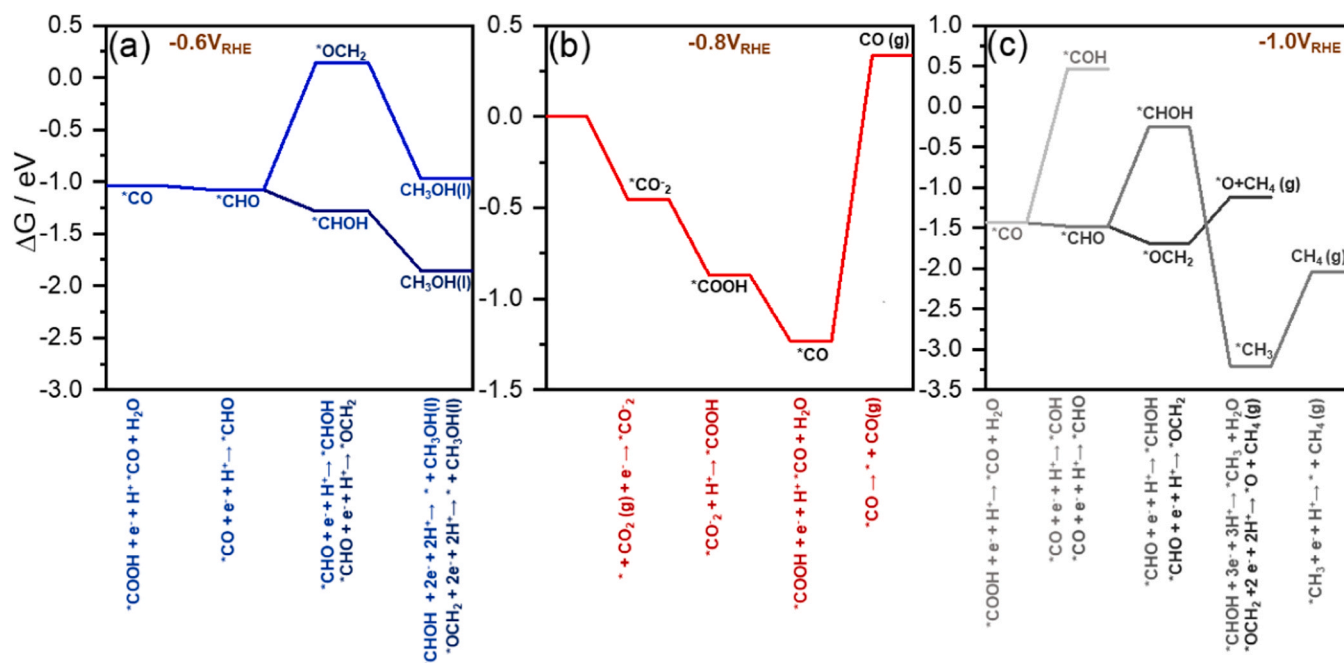


Fig. 6. CO electrocatalysis characterization. Mass spectroscopy (MS) analysis of CO electrocatalysis catholyte for the CoTPP/MWCNT composite.





**Fig. 7.** Gibbs free energy profiles for eCO<sub>2</sub>RR over CoTPP/MWCNT. (a) Towards CH<sub>3</sub>OH at -0.6 V<sub>RHE</sub>, (b) CO at -0.8 V<sub>RHE</sub>, and (c) CH<sub>4</sub> at -1.0 V<sub>RHE</sub> (pH = 6.8).

at elevated temperatures and high negative potential, there is a pathway for its production on CoTPP/MWCNT. These are from the reduction of CH<sub>3</sub>OH or alternatively CO<sub>2</sub> can be reduced to CH<sub>4</sub> through the \*CH<sub>2</sub>OH and \*CH<sub>3</sub> intermediates [51]. Both \*OCH<sub>2</sub> and \*CHOH are exergonic (Fig. S13) and hence, both would contribute to the total reaction.

The formation of CH<sub>4</sub> requires the presence of protons which can be produced by H<sub>2</sub>O reduction on the composite or H<sub>2</sub>O oxidation on the counter electrode followed by proton transport through the Nafion membrane. In this context, the MWCNT support may play a role by generating hydrogen as it is evident from CV in room temperature (Fig. 2a) that pristine nanotube quite actively promotes HER in N<sub>2</sub> environment. On this basis, the MWCNT surface is identified as an active site for HER with the energy of -1.26 eV at -0.6 V<sub>RHE</sub>. Thus, at higher temperature and potential it may provide hydrogen to facilitate CH<sub>4</sub> formation.

Finally, increasing temperature up to 30 °C seems to be favoring the production of CO and CH<sub>3</sub>OH. At the higher temperatures, the mass transport of CO<sub>2</sub> is improved which is tentatively attributed due to the modulation of surface tension of electrolyte, water dynamics, and decreased diffusion layer thickness [65–67].

#### 4. Conclusion

We present a joint study integrating experimental and theoretical methods to unravel (i) the improved activity of the CoTPP/MWCNT composite towards CH<sub>3</sub>OH formation at lower potentials (-0.6 V<sub>RHE</sub>), (ii) the temperature dependent products distribution favoring eCO<sub>2</sub>R products down to 30 °C and H<sub>2</sub> production at elevated temperatures and, (iii) employing temperature as a potential approach for controlling the ratio of CO and H<sub>2</sub> for syn-gas production. The improved activity of the composite is shown to originate from the strong CH-π interaction between CoTPP and electron conducting MWCNTs. Upon increasing temperature, decreasing oxygen containing product formation is observed whereas conversely increasing hydrogen rich product generation occurs. Notably, at -0.60 V<sub>RHE</sub> FE of CH<sub>3</sub>OH decreases with temperature and in contrary FE of CO increases which indicates that the temperature enhances the desorption of CO. Also, the efficiency of the competing HER increases with the increasing temperature and overpotential. The outstanding methanol production observed at 20 °C temperature and

low potential points toward an interface design to improve this product selectivity.

#### CRedit authorship contribution statement

**M.N. Hossain:** Conceptualization, Methodology, Formal analysis, Investigation, Writing – original draft, Writing – review & editing. **P. Prslja:** Conceptualization, Methodology, Investigation, Formal analysis, Writing – original draft, Writing – review & editing. **C. Flox:** Methodology, Writing – review & editing. **N. Muthuswamy:** Methodology, Writing – review & editing. **J. Sainio:** Investigation, Writing – review & editing. **A.M. Kannan:** Writing – review & editing. **M. Suominen:** Writing – review & editing. **N. Lopez:** Supervision, Writing – review & editing, Resources, Data curation. **T. Kallio:** Conceptualization, Methodology, Supervision, Writing – review & editing, Resources, Data curation.

#### Declaration of Competing Interest

The authors declare that they have no known competing financial interests or personal relationships that could have appeared to influence the work reported in this paper.

#### Acknowledgment

We are thankful for the financial support from the European Union under the project ELCOREL ITN Horizon 2020 (721624-ELCOREL), Academy of Finland (the Profi 5 project) and Jane and Aatos Erkko Foundation, Finland (the USVA project).

#### Appendix A. Supporting information

Supplementary data associated with this article can be found in the online version at doi:10.1016/j.apcatb.2021.120863.

#### References

- [1] P. De Luna, C. Hahn, D. Higgins, S.A. Jaffer, T.F. Jaramillo, E.H. Sargent, What would it take for renewably powered electrosynthesis to displace petrochemical processes? Science 364 (2019) <https://doi.org/10.1126/science.aav3506> (80–).

- [2] A. Boulamanti, J.A. Moya, Energy Efficiency and GH Emissions: Prospective Scenarios for the Chemical and Petrochemical Industry, 2017. (<https://doi.org/10.2760/20486>).
- [3] J.C. Minx, W.F. Lamb, M.W. Callaghan, S. Fuss, J. Hilaire, F. Creutzig, T. Amann, T. Beringer, W. De Oliveira Garcia, J. Hartmann, T. Khanna, D. Lenzi, G. Luderer, G.F. Nemet, J. Rogelj, P. Smith, J.L. Vicente Vicente, J. Wilcox, M. Del Mar Zamora Dominguez, Negative emissions – part 1: research landscape and synthesis, *Environ. Res. Lett.* 13 (2018), 063001, <https://doi.org/10.1088/1748-9326/aabf9b>.
- [4] K.P. Kuhl, E.R. Cave, D.N. Abram, T.F. Jaramillo, New insights into the electrochemical reduction of carbon dioxide on metallic copper surfaces, *Energy Environ. Sci.* 5 (2012) 7050–7059, <https://doi.org/10.1039/c2ee21234j>.
- [5] Y. Hori, Electrochemical CO<sub>2</sub> reduction on metal electrodes, in: C.G. Vayenas, R. E. White, M.E. Gamboa-Aldeco (Eds.), *Modern Aspects of Electrochemistry*, Springer, 2008, pp. 89–189, [https://doi.org/10.1007/978-0-387-49489-0\\_3](https://doi.org/10.1007/978-0-387-49489-0_3), accessed February 19, 2020.
- [6] D. Raciti, C. Wang, Recent advances in CO<sub>2</sub> reduction electrocatalysis on copper, *ACS Energy Lett.* 3 (2018) 1545–1556, <https://doi.org/10.1021/acsenenergylett.8b00553>.
- [7] Y.Y. Birdja, J. Shen, M.T.M. Koper, Influence of the metal center of metalloprotoporphyrins on the electrocatalytic CO<sub>2</sub> reduction to formic acid, *Catal. Today* 288 (2017) 37–47, <https://doi.org/10.1016/j.cattod.2017.02.046>.
- [8] G.F. Manbeck, E. Fujita, A review of iron and cobalt porphyrins, phthalocyanines and related complexes for electrochemical and photochemical reduction of carbon dioxide, *J. Porphyr. Phthalocyanines* 19 (2015) 45–64, <https://doi.org/10.1142/S1088424615300013>.
- [9] C. Diercks, S. Lin, Y.B. Zhang, C. Chang, O. Yaghi, Covalent organic frameworks comprising cobalt porphyrins for the electrocatalytic reduction of CO<sub>2</sub> in water, *Science* 349 (2015) 1208–1213 (80-).
- [10] N. Furuya, S. Koide, Electroreduction of carbon dioxide by metal phthalocyanines, *Electrochim. Acta* 36 (1991) 1309–1313, [https://doi.org/10.1016/0013-4686\(91\)80010-6](https://doi.org/10.1016/0013-4686(91)80010-6).
- [11] H. Aga, A. Aramata, Y. Hisaeda, The electroreduction of carbon dioxide by macrocyclic cobalt complexes chemically modified on a glassy carbon electrode, *J. Electroanal. Chem.* 437 (1997) 111–118, [https://doi.org/10.1016/S0022-0728\(97\)00386-0](https://doi.org/10.1016/S0022-0728(97)00386-0).
- [12] J.P. Collin, J.P. Sauvage, Electrochemical reduction of carbon dioxide mediated by molecular catalysts, *Coord. Chem. Rev.* 93 (1989) 245–268, [https://doi.org/10.1016/0010-8545\(89\)80018-9](https://doi.org/10.1016/0010-8545(89)80018-9).
- [13] A. Ghosh, A comparison of ortho, meta, and para substituent effects in tetraphenylporphyrins: insights into the nature of the porphyrin-phenyl electronic interaction, *J. Mol. Struct. THEOCHEM* 388 (1996) 359–363, [https://doi.org/10.1016/S0166-1280\(96\)80050-9](https://doi.org/10.1016/S0166-1280(96)80050-9).
- [14] C. Costentin, S. Drouet, M. Robert, J.M. Saveant, A.G. Yodh, H. Gleiter, J. Perepezko, M. Terrones, J.R. Dwyer, R.E. Jordan, R.J. Miller, M. Enomoto, J. K. Lee, F. Group, H.N. Lekkerkerker, D.G. Grier, E.R. Weeks, A. Schofield, P. N. Pusey, D.A. Weitz, D.W. Blair, A.J. Levine, R.A. Guyer, A.D. Dinsmore, A. M. Alsayed, A.G. Yodh, Y. Han, W. Van Megen, D.G. Grier, A. Dobry, H.T. Diep, L. Burakovsky, D.L. Preston, R.R. Silbar, G. Grimvall, Molecular Fe catalyst, *Science* 338 (2012) 90–94 (80-).
- [15] M. Zhu, D.T. Yang, R. Ye, J. Zeng, N. Corbin, K. Manthiram, Inductive and electrostatic effects on cobalt porphyrins for heterogeneous electrocatalytic carbon dioxide reduction, *Catal. Sci. Technol.* 9 (2019) 974–980, <https://doi.org/10.1039/c9cy00102f>.
- [16] J. Wang, S. Dou, X. Wang, Structural tuning of heterogeneous molecular catalysts for electrochemical energy conversion, *Sci. Adv.* 7 (2021) 1–14, <https://doi.org/10.1126/sciadv.abf3989>.
- [17] X.-M. Hu, M.H. Rønne, S.U. Pedersen, T. Skrydstrup, K. Daasbjerg, Enhanced catalytic activity of cobalt porphyrin in CO<sub>2</sub> electroreduction upon immobilization on carbon materials, *Angew. Chem. Int. Ed.* 56 (2017) 6468–6472, <https://doi.org/10.1002/anie.201701104>.
- [18] T.V. Magdesieva, T. Yamamoto, D.A. Tryk, A. Fujishima, Electrochemical reduction of CO[sub 2] with transition metal phthalocyanine and porphyrin complexes supported on activated carbon fibers, *J. Electrochem. Soc.* 149 (2002) D89, <https://doi.org/10.1149/1.1475690>.
- [19] C. Costentin, M. Robert, J.-M. Savéant, A. Tatin, Efficient and selective molecular catalyst for the CO<sub>2</sub> to-CO electrochemical conversion in water, *PNAS* 112 (2015), <https://doi.org/10.1073/pnas.1507063112>.
- [20] J. Shen, R. Kortlever, R. Kas, Y.Y. Birdja, O. Diaz-Morales, Y. Kwon, I. Ledezma-Yanez, K.J.P. Schouten, G. Mul, M.T.M. Koper, Electrocatalytic reduction of carbon dioxide to carbon monoxide and methane at an immobilized cobalt protoporphyrin, *Nat. Commun.* 6 (2015) 1–8, <https://doi.org/10.1038/ncomms9177>.
- [21] Y. Wu, Z. Jiang, X. Lu, Y. Liang, H. Wang, Domino electroreduction of CO<sub>2</sub> to methanol on a molecular catalyst, *Nature* 575 (2019) 639–642, <https://doi.org/10.1038/s41586-019-1760-8>.
- [22] E. Boutin, M. Wang, J.C. Lin, M. Mesnage, D. Mendoza, B. Lassalle-Kaiser, C. Hahn, T.F. Jaramillo, M. Robert, Aqueous electrochemical reduction of carbon dioxide and carbon monoxide into methanol with cobalt phthalocyanine, *Angew. Chem. Int. Ed.* (2019) 16172–16176, <https://doi.org/10.1002/anie.201909257>.
- [23] X. Zhang, Z. Wu, X. Zhang, L. Li, Y. Li, H. Xu, X. Li, X. Yu, Z. Zhang, Y. Liang, H. Wang, Highly selective and active CO<sub>2</sub> reduction electrocatalysts based on cobalt phthalocyanine/carbon nanotube hybrid structures, *Nat. Commun.* 8 (2017) 1–8, <https://doi.org/10.1038/ncomms14675>.
- [24] M.L. Waters, Aromatic interactions in model systems, *Curr. Opin. Chem. Biol.* 6 (2002) 736–741, [https://doi.org/10.1016/S1367-5931\(02\)00359-9](https://doi.org/10.1016/S1367-5931(02)00359-9).
- [25] W. Orellana, Catalytic activity toward oxygen reduction of transition metal porphyrins covalently linked to single-walled carbon nanotubes: a density functional study, *Phys. Rev. B* 84 (2011), 155405, <https://doi.org/10.1103/PhysRevB.84.155405>.
- [26] T. Mizuno, K. Ohta, A. Sasaki, T. Akai, M. Hirano, A. Kawabe, Effect of temperature on electrochemical reduction of high-pressure CO<sub>2</sub> with In, Sn, and Pb electrodes, *Energy Sources* 17 (1995) 503–508, <https://doi.org/10.1080/00908319508946098>.
- [27] Y. Hori, K. Kikuchi, A. Murata, S. Suzuki, Production of methane and ethylene in electrochemical reduction of carbon dioxide at copper electrode in aqueous hydrogen carbonate solution, *Chem. Lett.* 15 (1986) 897–898, <https://doi.org/10.1246/cl.1986.897>.
- [28] S. Tuomi, R. Guil-Lopez, T. Kallio, Molybdenum carbide nanoparticles as a catalyst for the hydrogen evolution reaction and the effect of pH, *J. Catal.* 334 (2016) 102–109, <https://doi.org/10.1016/j.jcat.2015.11.018>.
- [29] E.V. Basiuk, L. Huerta, V.A. Basiuk, Noncovalent bonding of 3d metal(II) phthalocyanines with single-walled carbon nanotubes: a combined DFT and XPS study, *Appl. Surf. Sci.* 470 (2019) 622–630, <https://doi.org/10.1016/j.apsusc.2018.11.159>.
- [30] C.S. Chen, A.D. Handoko, J.H. Wan, L. Ma, D. Ren, B.S. Yeo, Stable and selective electrochemical reduction of carbon dioxide to ethylene on copper mesocrystals, *Catal. Sci. Technol.* 5 (2015) 161–168, <https://doi.org/10.1039/c4cy00906a>.
- [31] G. Kresse, J. Furthmüller, Efficiency of ab-initio total energy calculations for metals and semiconductors using a plane-wave basis set, *Comput. Mater. Sci.* 6 (1996) 15–50, [https://doi.org/10.1016/0927-0256\(96\)00008-0](https://doi.org/10.1016/0927-0256(96)00008-0).
- [32] D. Joubert, From ultrasoft pseudopotentials to the projector augmented-wave method, *Phys. Rev. B Condens. Matter Phys.* 59 (1999) 1758–1775, <https://doi.org/10.1103/PhysRevB.59.1758>.
- [33] S. Grimme, J. Antony, S. Ehrlich, H. Krieg, A consistent and accurate ab initio parametrization of density functional dispersion correction (DFT-D) for the 94 elements H-Pu, *J. Chem. Phys.* 132 (2010), 154104, <https://doi.org/10.1063/1.3382344>.
- [34] J.P. Perdew, K. Burke, M. Ernzerhof, Generalized gradient approximation made simple, *Phys. Rev. Lett.* 77 (1996) 3865–3868, <https://doi.org/10.1103/PhysRevLett.77.3865>.
- [35] P.E. Blöchl, Projector augmented-wave method, *Phys. Rev. B* 50 (1994) 17953–17979, <https://doi.org/10.1103/PhysRevB.50.17953>.
- [36] H.J.M. James, D. Pack, Special points for Brillouin-zone integrations—a reply, *J. Chem. Inf. Model.* 16 (1977) 1748–1749.
- [37] A.A. Peterson, F. Abild-Pedersen, F. Studt, J. Rossmeisl, J.K. Nørskov, How copper catalyzes the electroreduction of carbon dioxide into hydrocarbon fuels, *Energy Environ. Sci.* 3 (2010) 1311–1315, <https://doi.org/10.1039/c0ee00071j>.
- [38] J.K. Nørskov, J. Rossmeisl, A. Logadottir, L. Lindqvist, J.R. Kitchin, T. Bligaard, H. Jónsson, Origin of the overpotential for oxygen reduction at a fuel-cell cathode, *J. Phys. Chem. B* 108 (2004) 17886–17892, <https://doi.org/10.1021/jp047349j>.
- [39] M. Álvarez-Moreno, C. De Graaf, N. López, F. Maseras, J.M. Poblet, C. Bo, Managing the computational chemistry big data problem: the ioChem-BD platform, *J. Chem. Inf. Model.* 55 (2015) 95–103, <https://doi.org/10.1021/ci500593j>.
- [40] P. Prslja <https://doi.org/10.19061/iochem-bd-1-209>.
- [41] M.A. Hoque, M. Gil-Sepulcre, A. de Aguirre, J.A.A.W. Elemans, D. Moonshiram, R. Matheu, Y. Shi, J. Benet-Buchholz, X. Sala, M. Malfois, E. Solano, J. Lim, A. Garzón-Manjón, C. Scheu, M. Lanza, F. Maseras, C. Gimbert-Surina, A. Llobet, Water oxidation electrocatalysis using ruthenium coordination oligomers adsorbed on multiwalled carbon nanotubes, *Nat. Chem.* 12 (2020) 1060–1066, <https://doi.org/10.1038/s41557-020-0548-7>.
- [42] M. Nishio, The CH/π hydrogen bond in chemistry. Conformation, supramolecules, optical resolution and interactions involving carbohydrates, *Phys. Chem. Chem. Phys.* 13 (2011) 13873–13900, <https://doi.org/10.1039/c1cp20404a>.
- [43] A.J. Neel, M.J. Hilton, M.S. Sigman, F.D. Toste, Exploiting non-covalent π interactions for catalyst design, *Nature* 543 (2017) 637–646, <https://doi.org/10.1038/nature21701>.
- [44] W. Ju, A. Bagger, X. Wang, Y. Tsai, F. Luo, T. Möller, H. Wang, J. Rossmeisl, A. S. Varela, P. Strasser, Unraveling mechanistic reaction pathways of the electrochemical CO<sub>2</sub> reduction on Fe-N-C single-site catalysts, *ACS Energy Lett.* 4 (2019) 1663–1671, <https://doi.org/10.1021/acsenenergylett.9b01049>.
- [45] A. Jorio, M.A. Pimenta, A.G. Souza Filho, R. Saito, G. Dresselhaus, M. S. Dresselhaus, Characterizing carbon nanotube samples with resonance Raman scattering, *New J. Phys.* 5 (2003) 139, <https://doi.org/10.1088/1367-2630/5/1/139>.
- [46] M.S. Dresselhaus, G. Dresselhaus, R. Saito, A. Jorio, Raman spectroscopy of carbon nanotubes, *Phys. Rep.* 409 (2005) 47–99, <https://doi.org/10.1016/j.physrep.2004.10.006>.
- [47] D.R. Roy, E.V. Shah, S. Mondal Roy, Optical activity of Co-porphyrin in the light of IR and Raman spectroscopy: a critical DFT investigation, *Spectrochim. Acta Part A Mol. Biomol. Spectrosc.* 190 (2018) 121–128, <https://doi.org/10.1016/j.saa.2017.08.069>.
- [48] L. Scudiero, D.E. Barlow, K.W. Hipps, Physical properties and metal ion specific scanning tunneling microscopy images of metal(II) tetraphenylporphyrins deposited from vapor onto gold, *J. Phys. Chem. B* (2000), <https://doi.org/10.1021/jp002292w>.
- [49] T. Lukaszczuk, K. Flechtner, L.R. Merte, N. Jux, F. Maier, J.M. Gottfried, H.-P. Steinru, Interaction of cobalt(II) tetraarylporphyrins with a Ag(111) surface studied with photoelectron, *Spectroscopy* (2007), <https://doi.org/10.1021/jp0652345>.
- [50] Y. Bai, F. Buchner, I. Kellner, M. Schmid, F. Vollnhals, H.P. Steinrück, H. Marbach, J.M. Gottfried, Adsorption of cobalt (II) octaethylporphyrin and 2H-

- octaethylporphyrin on Ag(111): new insight into the surface coordinative bond, *New J. Phys.* 11 (2009), 125004, <https://doi.org/10.1088/1367-2630/11/12/125004>.
- [51] M.C.O. Monteiro, L. Jacobse, T. Touzalin, M.T.M. Koper, Mediator-free SECM for probing the diffusion layer pH with functionalized gold ultramicroelectrodes, *Anal. Chem.* 92 (2020) 2237–2243, <https://doi.org/10.1021/acs.analchem.9b04952>.
- [52] R.M. Kellett, T.G. Spiro, Cobalt porphyrin electrode films as H<sub>2</sub> evolution catalysts, *Inorg. Chem.* 24 (1985) 2378–2382, <https://doi.org/10.1021/ic00209a012>.
- [53] D. Behar, T. Dhanasekaran, P. Neta, C.M. Hosten, D. Ejeh, P. Hambright, E. Fujita, Cobalt porphyrin catalyzed reduction of CO<sub>2</sub>. Radiation chemical, photochemical, and electrochemical studies, *J. Phys. Chem. A* (1998) 2870–2877, <https://doi.org/10.1021/jp9807017>.
- [54] N. Kornienko, Y. Zhao, C.S. Kley, C. Zhu, D. Kim, S. Lin, C.J. Chang, O.M. Yaghi, P. Yang, Metal-organic frameworks for electrocatalytic reduction of carbon dioxide, *J. Am. Chem. Soc.* 137 (2015) 14129–14135, <https://doi.org/10.1021/jacs.5b08212>.
- [55] M.E. Vol'pin, I.S. Kolomnikov, Reactions of carbon dioxide with transition metal compounds, *Coord. Chem.* (1973) 567–581, <https://doi.org/10.1016/b978-0-408-70470-0.50010-4>.
- [56] G.A. Olah, Towards oil independence through renewable methanol chemistry, *Angew. Chem. Int. Ed.* 52 (2013) 104–107, <https://doi.org/10.1002/anie.201204995>.
- [57] X. Nie, M.R. Esopi, M.J. Janik, A. Asthagiri, Selectivity of CO<sub>2</sub> reduction on copper electrodes: the role of the kinetics of elementary steps, *Angew. Chem. Int. Ed.* 52 (2013) 2459–2462, <https://doi.org/10.1002/anie.201208320>.
- [58] K.P. Kuhl, T. Hatsukade, E.R. Cave, D.N. Abram, J. Kibsgaard, T.F. Jaramillo, Electrocatalytic conversion of carbon dioxide to methane and methanol on transition metal surfaces, *J. Am. Chem. Soc.* 136 (2014) 14107–14113, <https://doi.org/10.1021/ja505791r>.
- [59] A. Bagger, W. Ju, A.S. Varela, P. Strasser, J. Rossmeisl, Electrochemical CO<sub>2</sub> reduction: a classification problem, *ChemPhysChem* 18 (2017) 3266–3273, <https://doi.org/10.1002/cphc.201700736>.
- [60] X.-M. Hu, M.H. Rønne, S.U. Pedersen, T. Skrydstrup, K. Daasbjerg, Enhanced catalytic activity of cobalt porphyrin in CO<sub>2</sub> electroreduction upon immobilization on carbon materials, *Angew. Chem. Int. Ed.* 56 (2017) 6468–6472, <https://doi.org/10.1002/anie.201701104>.
- [61] N.M. Marković, T.J. Schmidt, B.N. Grgur, H.A. Gasteiger, R.J. Behm, P.N. Ross, Effect of temperature on surface processes at the Pt(111) – liquid interface: hydrogen adsorption, oxide formation, and CO oxidation, *J. Phys. Chem. B* 103 (1999) 8568–8577, <https://doi.org/10.1021/jp991826u>.
- [62] E. Herrero, J.M. Feliu, S. Blais, Z. Radovic-Hrapovic, G. Jerkiewicz, Temperature dependence of CO chemisorption and its oxidative desorption on the Pt(111) electrode, *Langmuir* 16 (2000) 4779–4783, <https://doi.org/10.1021/la9907432>.
- [63] F. Zhang, A.C. Co, Direct evidence of local pH change and the role of alkali cation during CO<sub>2</sub> electroreduction in aqueous media, *Angew. Chem. Int. Ed.* 59 (2020) 1674–1681, <https://doi.org/10.1002/anie.201912637>.
- [64] N. Gupta, M. Gattrell, B. MacDougall, Calculation for the cathode surface concentrations in the electrochemical reduction of CO<sub>2</sub> in KHCO<sub>3</sub> solutions, *J. Appl. Electrochem.* 36 (2006) 161–172, <https://doi.org/10.1007/s10800-005-9058-y>.
- [65] M. König, J. Vaes, E. Klemm, D. Pant, Solvents and supporting electrolytes in the electrocatalytic reduction of CO<sub>2</sub>, *IScience* 19 (2019) 135–160, <https://doi.org/10.1016/j.isci.2019.07.014>.
- [66] N.B. Vargaftik, B.N. Volkov, L.D. Voljak, International tables of the surface tension of water, *J. Phys. Chem. Ref. Data* 12 (1983) 817–820, <https://doi.org/10.1063/1.555688>.
- [67] C.F.C. Lim, D.A. Harrington, A.T. Marshall, Effects of mass transfer on the electrocatalytic CO<sub>2</sub> reduction on Cu, *Electrochim. Acta* 238 (2017) 56–63, <https://doi.org/10.1016/j.electacta.2017.04.017>.